Journal of Applied Fluid Mechanics, Vol. 16, No. 2, pp. 205-221, 2023.
Available online at www.jafmonline.net, ISSN 1735-3572, EISSN 1735-3645.
https://doi.org/10.47176/jafm.16.02.1296

Experimental and Computational Study on Effect of Vanes on Heat Transfer and Flow Structure of Swirling Impinging Jet

S. M. Illyas[1†], A. MuthuManokar[1] and A. E. Kabeel[2, 3]

[1]*Department of Mechanical Engineering, B S Abdur Rahman Crescent Institute of Science and Technology, Chennai - 600048, India*
[2]*Mechanical Power Engineering Department, Faculty of Engineering, Tanta University, Tanta - 31527, Egypt*
[3]*Faculty of Engineering, Delta University for Science and Technology, Gamasa - 35712, Egypt*

†*Corresponding Author Email: illyas@bsauniv.ac.in*

(Received May 9, 2022; accepted October 8, 2022)

ABSTRACT

The study focuses on heat transfer performance and flow structure associated with swirling jet on a flat target surface. The analysis is carried out with helicoid inserts of swirl number S = 1.3 by varying the number of vanes with Reynolds number between 11200 and 35600. The comparison of swirling jet with circular jet is carried out on its heat transfer performance. The heat transfer and flow structure are visualized using thermo-chromic liquid crystal sheet and oil film technique respectively. The numerical simulation is also performed at Re = 24700 for H/D distance between 1 and 4 using computational fluid dynamics. The heat transfer results reveal that the presence of axial recirculation zone at Re = 29800 and 35600 for the triple helicoid affects the uniformity of heat transfer distribution at $0 < X/D < 1.5$ at H/D = 3. The axial component of velocity with respect to swirling jet is less than zero in the stagnation area and it increases at $0.57 < r/D < 0.97$ for single vane and $0.63 < r/D < 0.97$ for double and triple vanes. While the steep increase in tangential velocity of the triple vane jet is apparent at $0 < r/D < 0.5$ at H/D = 2 and 3, the maximum value of point radially shifts inward towards the jet. The location of maximum turbulent kinetic energy approaching the surface at about r/D = 0.9 - 1.2 which characterizes the swirling jet at H/D = 2.

Keywords*:* Heat transfer; Thermochromic liquid crystal; Swirling jet; CFD; Flow characteristics.

NOMENCLATURE

A	area of impinging surface	q_{in}	heat input
D	pipe exit diameter	$T_w(r)$	temperature on the impinging surface at radius r from the center
H/D	non-dimensional distance between exit of jet and impinging plate	T_j	temperature of air at the outlet of main pipe
h	convective heat transfer coefficient	T_a	ambient temperature
k_a	thermal conductivity of air	U_0	mean velocity
Nu	Nusselt number	u	axial velocity
Re	Reynolds number	u_t	tangential velocity
r/D	non-dimensional radial distance on the impinging surface		

1. INTRODUCTION

Impinging jets are being used in the applications like cooling of electronic components, turbine blades and drying of food products. In such applications high heat transfer rate with uniformity is required. The impinging jet offers effective use of fluid and higher transfer rates comparing to other heat transfer applications not employing phase change. The much higher heat transfer coefficient is due to local thinning of impingement boundary layer enables higher surface heat transfer rate. The reported studies

of impinging jet heat transfer shows that an extensive variation in convective heat transfer coefficients for identical experimental parameters. The studies on impinging jet can be classified according to the jet leaving the nozzle as circular jet, slotted jet and swirling jet (Zuckerman and Lior 2006). Fleischer *et al.* (2001) visualized the vortices development in a circular impinging jet by employing a smoke wire technique and reported that the vortices break up at the end of the potential core region prior to the impingement at larger separation (H/D = 4) distances. They reported that magnitude of vorticity is not only influenced by the local swirling motion but also by shear. Vortices affect the spreading of jet, size of potential core and entrainment depending on their extent and strength. They concluded that vortices break up rapidly at smaller separation (H/D = 1) distances following the impingement due to separation from the impinging surface. Lytle and Webb (1994) observed the accelerated flow at very low nozzle to plate spacing (H/D = 0.1) rising the turbulence intensity near at r/D ≈ 0.75. They reported that the shear layer interaction with stagnant ambient air likely the causes for considerable rise in the turbulence level for small H/D distances which would have an intense effect on local heat transfer. The study by Goldstein and Timmers (1982) carried out heat transfer studies on array of circular impinging jet (Re = 40000 and H/D = 2 and 6) reporting that flow interaction of multiple jet causes mixing induced turbulence to penetrate further towards individual jet center resulting in minimum Nusselt number at the center of the jet rather than the outer ones of three co linear jets compared with array of seven jets. Tang *et al*. (2021) carried out numerical analysis on heat transfer and flow structure of the round jet on a cylindrical cavity heat sink with varying diameter and jet exit impinging surface distance. They reported that the cylindrical cavity enhances the heat transfer rate of the heat sink and the horse shoe vortex produced near the cavity edge improves the heat transfer performance.

Qiu *et al*. (2019) focused on heat transfer on flow characteristics of slotted jet on concave surface by varying the Jet to target spacing (H/B ratio =1-2.2), surface curvature (R/B = 4- 20) with Reynolds number range of 8000 and 40000. Their results reveal that Nusselt number is increasing at smaller curvature (4- 15) and it decreases when the curvature is larger (>15). They reported decreased heat transfer with the increase H/B ratio. Shukla and Dewan (2017) examined the heat transfer performance of slotted impinging jet on a ribbed surface. The reported the capability of standard k-w and sst – kw models in predicting the secondary peak Nusselt number. They analyzed the effect of rib to plate clearance and rib position and concluded that increasing rib clearance and rib position in streamwise direction enhances the heat transfer. Bentarzi *et al.* (2019) compared heat transfer performance of perpendicular impinging jet with twin jets of parallel, convergent and divergent arrangements. Their findings reveal that the position of peak Nusselt number and its magnitude varies due variation stagnation point with increasing angle of impingement from 0° to 60°. They reported that heat transfer is relatively higher in the perpendicular impinging jet compared with oblique jet. Gioacchino *et al.* (2014) examined the performance of jet with fractal pattern and square pattern. They reported that fractal pattern increases heat transfer rate in the impinging area in the order greater than 63%, whereas the regular pattern achieves as low as 9% at H/D ≤ 2. The heat transfer performance of fractal pattern drops down drastically in the stagnation region for larger jet exit to surface distance (H/D = 4).

Kinsella *et al.* (2008) analyzed the heat transfer characteristic of a jet over a horizontal surface (Re = 10000 - 30000) for the jet exit distance of 0.5 to 6. Their results showed that that the heat transfer at the stagnation region is reduced at low jet exit distance due to the swirling effect and the optimum intensity of swirl for heat transfer enhancement depends on the separation distance. Huang and Yang (2005) showed that the higher swirl enhances the turbulence and flame speed thereby reducing the flame surface area without affecting the net heat release rate. Park and shin (1993) visualized the entrainment characteristics of swirling jet and reported that the entrainment rate increases with increasing swirl intensity. The intensity of the swirl significantly influences the size and recirculation zone. Ianiro and Cardone (2012) used swirl producing device of Sw = 0 - 0.8 for their heat transfer study at Re = 28000 and reported that the swirling flow creates axial pressure gradient that becomes intense with increasing swirl number causing breakdown of vortex core at the centre of the jet resulting in recirculation region characterized by low heat transfer rate. Illyas *et al.* (2019) performed experimental analysis on Nusselt number variation and optimization study of jet with intense swirling effect. They used helicoid inserts of swirl number 0.75 and 1.1 with varying H/D distances (1- 4) for the different Reynolds numbers (12700 – 32700). Their results showed that jet with swirling effect provides heat transfer uniformity over the target plate compared with circular jet. Ichimiya and Tsukamoto (2010) analyzed the Nusselt number variation of jet at Re = 1900. Their study revealed that flow speed and mixing at the vicinity of the impinging surface through swirl improve heat transfer, whereas recirculating flow decrease the heat transfer.

Based on the literature review presented in the Table 1, the studies on impinging jet is limited with swirl number of 1 and to the authors' best knowledge the studies carried out by Illyas *et al.* (2019) and Ichimiya and Tsukamoto (2010) have focused on swirl number 1.1 and 1.18 respectively. According to the study conducted by Ianiro and Cardone (2012) for the swirl number Sw = 0 - 0.8, the higher swirl number produces stronger axial recirculation zone which significantly affects the heat transfer performance and flow structure. Therefore, it is essential to understand the influence of higher swirl number with varying number of vanes on heat transfer and flow characteristics. As a result the present study focuses on heat transfer and flow structure of the jet for swirl number of 1.3 with single, double and triple vanes. The analysis includes

Table 1 – The summary of literature on impinging jet and parameters investigated

S.No	Literature	Type of Jet	Reynolds number	Impinging surface	Parameters investigated
1	Lytle and Webb (1994)	Circular jet	3600 – 27600	Flat surface	z/D = 0.1 – 1 *Nu* u, u_{RMS}
2	Tang *et al.* (2021)	Circular jet	5000 -23000	Cylindrical cavity	d/D = 2,3,4 H/D = 0.05 – 0.2 *Nu*
3	Fleischer *et al.* (2001)	Circular Jet	6000 - 15000	Convex surface	H/D = 1- 4 d/D = 0.18 – 0.38
4	Goldstein and Timmers (1982)	Circular Jet (single and multi-channels)	40000	Flat surface	H/D = 2,6 *Nu* Single and co-linear jets
5	Geers *et al.* (2008)	Circular Jet (multi-channel)	5000 - 20000	Flat surface	H/D = 3, 10 S/D = 2,6 *Nu* Inline and Hexagonal
6	Qui *et al.* (2017)	Slotted jet	8000 -4000	Concave surface	H/B = 1 -2.2 *Nu*, u'/u^2
7	Shukla and Dewan (2017)	Slotted Jet	5500 - 2000	Flat surface	H/B = 4 C/B = 0 - 0.2 *Nu*
8	Bentarzi *et al.* (2019)	Slotted Jet	5000 - 11000	Flat surface	*Nu*, D/W = 8 H/W = 20 α = 0°- 60°
9	Giocchino *et al.* (2014)	Slotted Jet	16000 - 28700	Flat surface	H/D = 1- 4, r/D = 0 – 5 Z/D = 0 – 1 Q = 0.9 mW – 4.7 mW
10	Ianiro and Cardone (2012)	Swirling Jet	28000	Flat surface	*Nu* X/D = 2-10 *Sw* = 0-0.8
11	Ichimiya and Tsukamoto (2010)	Swirling Jet	1900	Flat surface	*Sw* = 0.31, 0.61,1.08 H/D = 1.4, T
12	Fenot *et al.* (2015)	Swirling Jet	23000 - 30000	Flat surface	*Sw* = 0 – 0.26 H/D = 1 – 3 *Nu*, u/u_0
13	Kinsella *et al.* (2008)	Swirling Jet	10000 -30000	Flat surface	S = 0 -2.25°/mm H/D =0.5 – 6
14	Wannasi and Mannoyer (2015)	Swirling Jet (multi-channel)	27000	Flat surface	S/D = 5 Inline and Staggered H/D = 4 *Nu* θ = 20°,30°, 45°
15	Cafiero *et al.* (2014)	Fractal Jet	28700	Flat surface	H/D = 2 - 4 Nu
16	Chandramohan *et al.* (2017)	Swirling Jet	18000 - 22000	Flat surface	H/D = 2,4,6 Nu Q = 7667 W/m^2
17	Chung and Luo (2002)	Circular Jet	300 -1000	Flat surface	Nu, $Nu_{stag,}$ Vorticity
18	Sheen *et al.* (1996)	Swirling Jet	60- 6000	Flat surface	X/D = 1- 4 θ = 0° - 56° Nu, u/u_o,
19	Tangirala *et al.* (1987)	Swirling Jet	20000	Flat surface	*Sw* = 0 – 4 H/D = 1- 14 U_0
20	Yazdabadi *et al.* (1994)	Swirling Jet	14250 – 42750	Flat surface	*Sw* = 1.79 – 3.04 U, θ

comprehensive flow characteristics study on axial velocity, tangential velocity, turbulence kinetic energy and velocity vectors. The study includes heat transfer performance and flow structure of circular and swirling jets with single, double and triple vanes of swirl number, S = 1.3 for Re = 11200 - 35600 at H/D = 1-4. The present study can be used for the applications where the heat transfer enhancement with uniform cooling is preferred such as cooling of electronic components, tempering of glass, drying of fabrics and food products.

2. EXPERIMENTAL METHODOLOGY

2.1 Experimental Setup of an Impinging Jet Facility

The experimental setup consists of a centrifugal blower delivering air to a converging pipe. The air is supplied to a main pipe connected with a heating coil and flow measuring device as shown in Fig. 1. The mass flow of air can be adjusted by a gate valve connected with a converging pipe. The air temperature is maintained uniformly in the smooth pipe using a heater and temperature controller. The impinging section was made of a heater, metal foil and TLC sheet. The test section was composed of a stainless steel sheet with a thickness of 0.03 mm and a width and length of 300 mm each. Screws are provided to secure the stainless steel foil and thin heating sheet to the surface of the acrylic plate. The TLC sheet (300 mm × 300 mm x 0.1 mm) is glued over the stainless steel foil to prevent air bubbles from forming. Through the use of a heater sheet and a DC power supply unit, heat is applied to the metal foil. The varying power supply unit with the precision controls allows the heat flux to be imposed while keeping the working temperature of TLC sheet sheet within a limited range between 35°C and 49°C. The swirling inserts used in this study are single, double and triple vanes of swirl number S = 1.3 as shown in Fig. 2 b. The vane diameter is 30 mm and hub diameters is 8 mm. The length of the helicoid insert is 200 mm and the vane angle is 61°.The swirl number referring to the degree of swirl generated is obtained from the following equation given by Gupta et al. (1984)

$$S = \frac{2}{3}\left[\frac{1-\left(\frac{D2}{D1}\right)^3}{1-\left(\frac{D2}{D1}\right)^2}\right] tan\ \theta \quad (1)$$

Where, D_1 and D_2 are the hub and vane diameters of the helicoid insert. θ is the vane angle.

2.2 Calibration of Liquid Crystal Sheet

The TLC sheet supplied by Hallcrest of R35C5W which refers to red at 35°C and blue at 40°C.

The working temperature is varying between 35°C and 49°C. The calibration test plate is comprised of an acrylic plate with dimensions of 400 × 400 x 12 mm that holds the aluminium plate, thin heater sheet, and TLC sheet (Fig. 3). The thermocouples are positioned in the grooves on an Aluminium plate surface of dimensions 300 mm x 300 mm x 3 mm. The temperature along the surface of the Aluminium plate is measured using eight thermocouples with thin leads. The thermocouple leads are connected to the NI 9213 input module and subsequently connected to the computer system. The average temperature of the aluminium plate is measured

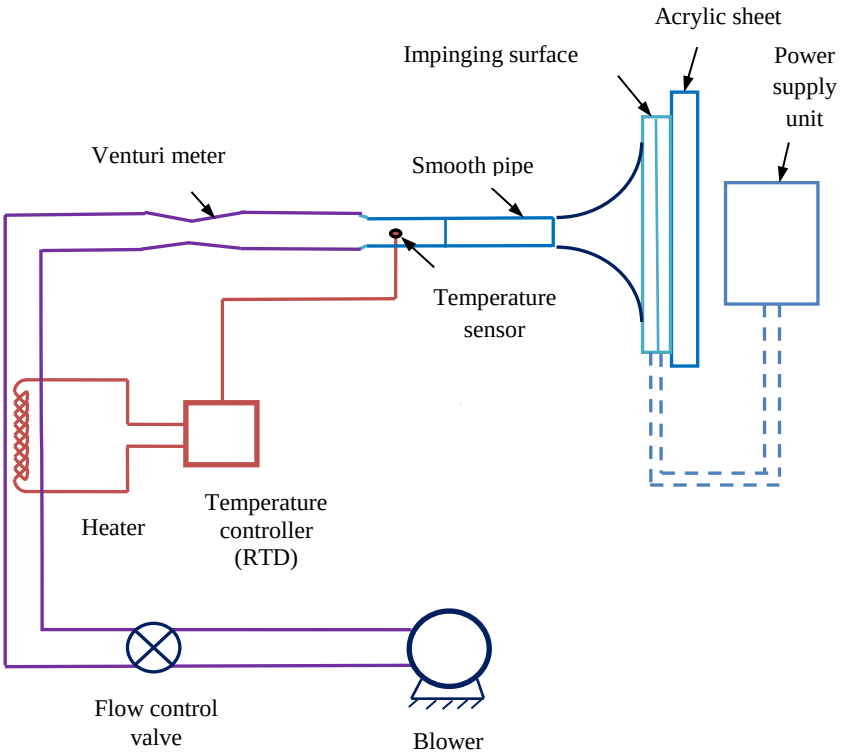

Fig. 1. Schematic of experimental setup.

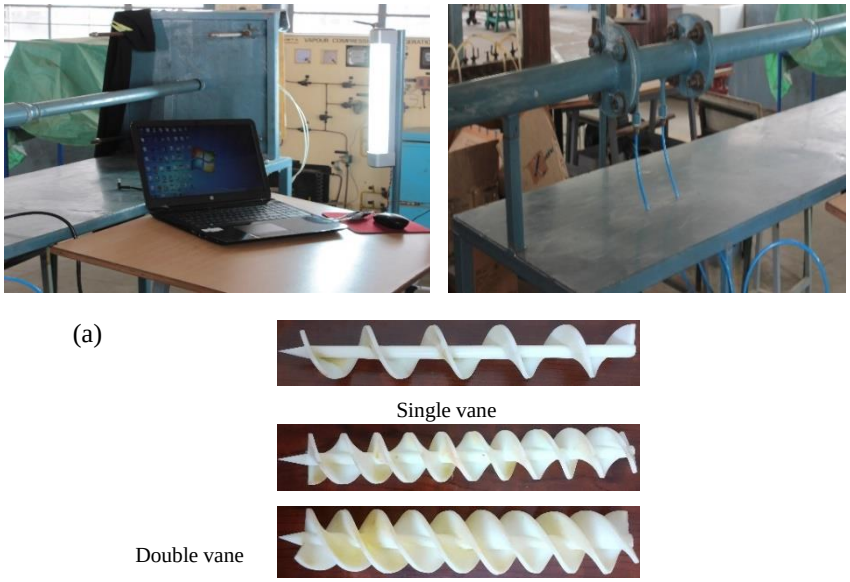

Fig. 2. (a) Photograph of the experimental setup (b) Helicoid vanes of swirl number *S* = 1.3.

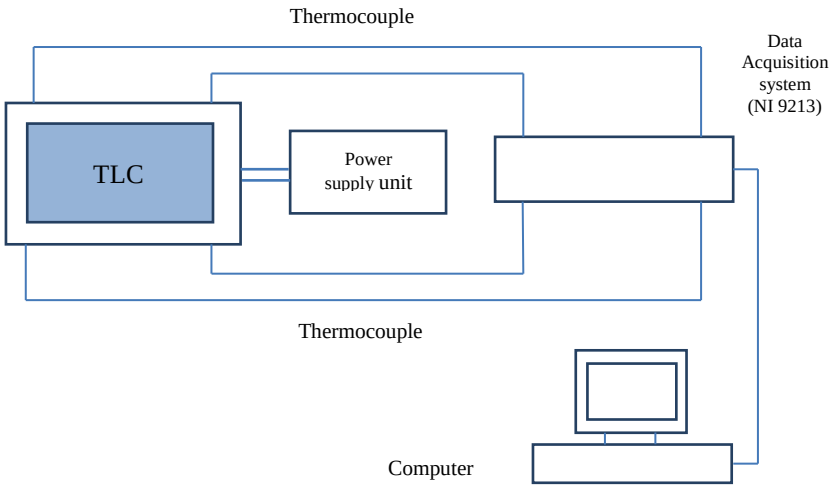

Fig. 3. Schematic of the calibration setup.

using thermocouples and a data acquisition system while it is gradually heated from 35°C to 49°C. The fine control modules of the DC power supply system enable to deliver heat in small incremental stages. When the temperature achieves a steady state, the change of color TLC and the temperature are both recorded at the same time. The RGB color pattern of the images is transformed into HSI domain, and its HSI values are extracted using the Measurement Statistics function of the Vision Assistant module in *Lab view*. As a result, the hue variation of the TLC sheet with reference to temperature variation is drawn as shown in Fig. 4. As the TLC color variation is significantly related to the temperature corresponding to the hue values between 0.534 and 0.687 (Fig. 4) are considered to be the region of interest for the change of color of TLC. The calibration curve's polynomial fit is utilized to connect the temperature and color value. Using the correlation, the surface temperature is calculated from the color values of TLC.

2.3 Test Section for Flow Visualization

The oil film visualization method is employed in the present analysis. The test plate consists of an acrylic sheet (450 mm x 450 mm x 10 mm) painted with a liquid mixture mounted over the guide screws thereby directly facing the impinging jet. A digital camera (Canon EOS 500 D) is used to capture the images of the flow pattern of the impinging jet and subsequently stored in the computer. The liquid mixture is prepared with paraffin liquid, titanium dioxide and oleic acid. It is coated on the impinging plate to produce an oil film. The flow pattern exposed to the jet is recorded by a camera for every 30 seconds during a period of 3 minutes for each trial.

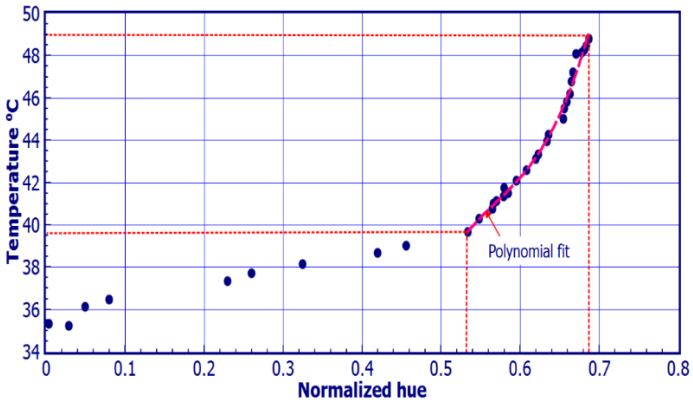

Fig. 4. Hue versus temperature for calibration of TLC sheet.

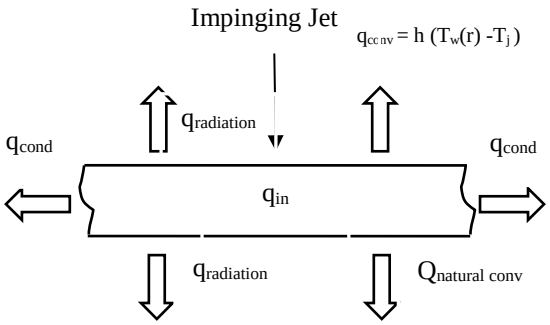

Fig. 5. Energy balance on the impinging surface.

2.4 Data Reduction

The heat transfer balance on the plate (Fig. 5) is used to calculate the convective heat transfer coefficient and Nusselt number by convective heat transfer. They are evaluated according to Eiamsa-ard *et al.* (2015) using the Eqs. (2) and (3) respectively.

$$h = \frac{q_{in} - q_{cond} - q_{natural\ conv} - q_{rad}}{(T_w(r) - T_j)} \tag{2}$$

$$Nu = \frac{h\,D}{k_a} \tag{3}$$

The conduction heat transfer on the impinging surface due to temperature gradient is given as (Eiamsa-ard *et al.* 2015)

$$q_{cond} = (k_s\, t_s + k_T\, t_T)\left(\frac{\partial^2 T}{\partial x^2} + \frac{\partial^2 T}{\partial y^2}\right) \tag{4}$$

The conductivity of foil sheet and TLC (k_T = 0.25 W/m K - Ahlers *et al.* 1994) are denoted by k_s and k_T respectively and the thickness of stainless steel and TLC sheet are represented by t_s and t_T . While the temperature gradient on the surface of the stainless steel is assumed to be negligible as it is extremely thin (0.03 mm), the heat conduction along the surface of the TLC (300 mm x 300 mm) in *x* and *y* axes is evaluated with the obtained temperature at predetermined locations and subsequently q_{cond} is calculated.

The free convection loss can be evaluated from the equation according to Holman (2002),

$$q_{natural\ conv} = h_{natural\ conv}\,(T_s - T_a) \tag{5}$$

Where $h_{natural\ conv}$ is convection coefficient, T_s is the surface temperature of the target surface and T_a is ambient temperature.

The heat loss due to radiation according to Geers *et al.* (2008) is given by

$$q_{radiation} = \sigma_{st}\,\epsilon_T\,(T_s^4 - T_a^4) \tag{6}$$

Where σ_{st} and ϵ_T denote the Stefan Boltzmann's value and emissivity of the sheet respectively. While the radiation and natural convection losses are calculated as 9.52% and 7.78% of the imposed heat and conduction heat loss is estimated as 2.85%.

2.5 Uncertainty Analysis

Kline-Mc Clintock method (Holman, 2002) is used for uncertainty analysis and the following equation is used

$$\Delta R = \left[\left(\frac{\partial R}{\partial m_1}\right)^2 (\Delta\epsilon_1)^2 + \left(\frac{\partial R}{\partial m_2}\right)^2 (\Delta\epsilon_2)^2 + \ldots\ldots \left(\frac{\partial R}{\partial m_n}\right)^2 (\Delta\epsilon_n)^2\right]^{1/2} \tag{7}$$

where m is the measured variable which can be directly measurable such as heat supplies (Q), target surface area (A), target surface temperature (T_s) and the jet exit temperature (T_j).

The derived variable (R) represents the quantity of interest that needs to be estimated by using an appropriate relation involving several directly measured variables such as convective heat transfer coefficient (h) and $\Delta\epsilon$ is the error in the measured quantity. The derived and measured variables can be substituted in Eq. (7) and the uncertainty in Nusselt number (ΔNu) is given by

$$\left[\left(\frac{\partial Nu}{\partial q_{in}}\right)^2(\Delta\epsilon_q)^2+\left(\frac{\partial Nu}{\partial D}\right)^2(\Delta\epsilon_D)^2+\left(\frac{\partial Nu}{\partial T_{w\,(r)}}\right)^2(\Delta\epsilon_{T_w})^2+\left(\frac{\partial Nu}{\partial T_j}\right)^2\left(\Delta\epsilon_{T_j}\right)^2\right]^{\frac{1}{2}} \quad (8)$$

here, $Nu = \frac{q\,D}{k_a\,(T_{w\,(r)} - T_j)}$ and k_a is assumed to be constant

After substituting Nu in Eq. (8) and simplifying the uncertainty in Nusselt number (ΔNu) is given by

$$\left[\left(\frac{D}{k_a\,(T_{w\,(r)} - T_j)}\right)^2(\Delta\epsilon_q)^2+\left(\frac{q}{k_a\,(T_{w\,(r)} - T_j)}\right)^2(\Delta\epsilon_D)^2+\left(\frac{q\,D}{-k_a\,T_{w\,(r)^2}}\right)^2(\Delta\epsilon_{T_w})^2+\left(\Delta\epsilon_{T_j}\right)^2\right]^{\frac{1}{2}} \quad (9)$$

and error level in q is calculated using the following equation

$$\left[\left(\frac{\partial q}{\partial V}\right)^2(\Delta\epsilon_v)^2+\left(\frac{\partial q}{\partial I}\right)^2(\Delta\epsilon_I)^2+\left(\frac{\partial q}{\partial A}\right)^2(\Delta\epsilon_A)^2\right]^{\frac{1}{2}} \quad (10)$$

where $q = \frac{V\,I}{A}$

The uncertainty value of Nusselt number for a single vane is calculated as 6.23% at H/D = 4 for Re = 11200.

3. NUMERICAL STUDY

Figure 6 shows the domain considered for the numerical study and boundary conditions. The swirl holding pipe is placed at a distance of H above the impinging surface where the jet impinges while it leaves the pipe as a swirling jet. The tetrahedral and prism elements are used to discretize the domain. Considering air as a working fluid the boundary condition at the inlet is provided with uniform velocity. The exit boundary condition is given with a pressure of 1 atm. The bottom surface of the domain where the jet impinges is provided with prescribed uniform heat flux wall boundary conditions. The top surfaces of the domain and pipe outer surface are considered as confined walls in accordance with the experimental set up are assigned with no slip adiabatic wall boundary conditions as shown in Fig. 6 a. Numerical analysis is performed by using Ansys CFX. The SST – k ω turbulence model is used in the present analysis as flow involves rotation and recirculation according to Liu *et al.* (2015). The simulation is performed based on the fluid flow equations namely continuity, momentum and energy equations plus an appropriate turbulence model as a closure. The equations for incompressible flow according to Versteeg and Malalasekara (1995) and Tannehill *et al.* (1997) in Cartesian coordinates are given as follows. The continuity equation is given as

$$\nabla.\bar{V} = 0 \quad (11)$$

where $\bar{V} = (u, v, w)$ is the velocity field

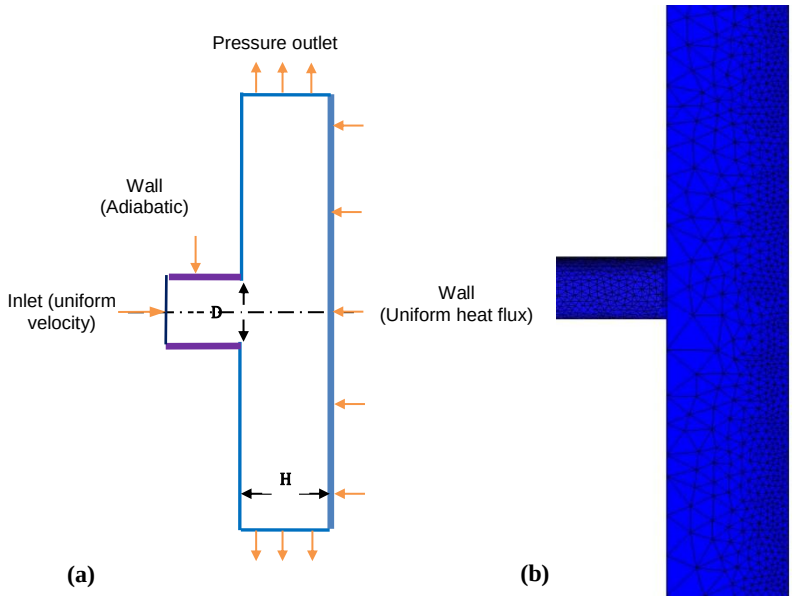

Fig. 6 (a) Computational domain (b) Discretized domain showing fine grid elements near the impinging plate.

and momentum equation is given as,

$$\rho \frac{D\bar{V}}{Dt} = \rho f - \nabla p + \mu \nabla^2 \bar{V} \quad (12)$$

while the first term (ρf) on RHS in Eq. 12 refers to body forces and the second term (∇p) refers to pressure forces, whereas the term $\mu \nabla^2 \bar{V}$ denotes the viscous forces. The LHS is the rate of change of momentum per unit volume describing the momentum change that any element experiences as it moves between zones of different velocities in the flow field.

Energy equation is given as,

$$\rho \frac{De}{Dt} = \frac{\partial Q}{\partial t} + k\nabla^2 \mathrm{T} + \varphi \quad (13)$$

The term $\rho \frac{De}{Dt}$ on LHS represents the rate of change in energy and the term $\frac{\partial Q}{\partial t}$ on the rate of heat generation and term $k\nabla^2 \mathrm{T}$ represents (rate of heat diffusion) rate of heat transfer by conduction and φ is (viscous dissipation) dissipation function denoting the rate at which mechanical energy is expended in the deformation process of a fluid due to viscosity (Tannehill *et al.* 1997). Grid independency study is carried out for validating the numerical results. The grid numbers are varied from a value of 1.76 million to 6.91 million (fine grid structure). The Table 2 shows the turbulent kinetic energy variation for double helicoid at *Re* = 24700 in the area of *r/D* between 0.5 and 2 where the turbulence fluctuations are higher. The relative deviation of turbulent kinetic energy is marginal between GF 5 and GF 6 showing that increasing nodes greater than GF 5 will have minimal effect. Hence the number of nodes corresponding to GF 5 is chosen for the present study.

Table 2 – Turbulence kinetic energy variation for different grid elements

Grid factor	Grid Nodes, Million	u^l/U_o^2	Deviation of u^l/U_o^2 compared with GF 6%
GF1	1.76	0.0663	3.634
GF2	2.47	0.0671	2.471
GF3	3.68	0.0678	1.453
GF4	5.01	0.0681	1.017
GF5	6.78	0.0684	0.581
GF 6	6.91	0.0688	---

4. EXPERIMENTAL RESULTS

4.1 Heat transfer and flow visualization

The Nusselt number variation at *H/D* = 2 and 3 is shown in Figures 7 and 8. The circular jet shows the existence of potential core at jet exit with uniform velocity indicating relatively less jet spread prior to the impingement as shown in Fig. 7 a. The swirling jet of single vane producing higher Nusselt number in the area at *X/D* is between 0 and 1.5 and *Y/D* is between 0 and 1.5 for *Re* = 11200 and the intensity increases with a rise in Reynolds number (Fig. 7 b). The jet profile leaving the double and triple vanes, which have significantly greater Nusselt numbers in the wall jet zone, is shown by the Nusselt number distribution. The Nusselt number for triple vanes has significantly lower value, indicating that the number of vanes has a major impact on the formation of axial recirculation area near the middle part of the target plate (Fig. 7 c). The Nusselt number distribution for triple vane (Fig.7 c) is particularly higher at *X/D* values between 1 and 3 in the Reynolds number range between 18400 and 35600 in comparison with other vanes (Fig.7 c) at *H/D* = 2. This fact indicates that multiple jets leaving triple vane entrains ambient air causing greater value of heat as shown by Huang and El-Genk (1998). But the variation of Nusselt number is marginal at *Re* = 11200 and 18400 among the single, double and triple vanes for *H/D* = 2 (Fig. 7). At H/D = 3, the value of the Nusselt number on the impinging surface is considerably smaller (Fig.8). This is because of the jet's decreased momentum as the target surface distances increases. Besides at lower Reynolds number (11200 and 18400) the Nusselt number distribution is nearly similar up to *X/D* = 1.5 for swirling jets (Fig.8). The flow streams of jet on plate are shown in Fig.9 and 10 at *H/D* = 2 and 3. While the black zone representing the oil film removed area and the white zone represents an unremoved film zone. The degree of jet spread and turbulence are observed to increase significantly with increasing number of vanes as it can be seen as a broadened impingement area for the swirling jet (Fig. 9 b, c and d). This fact indicates the possible enhanced mixing and entrainment of jet with ambient air before impingement as reported by Park and shin (1993). There appears a stagnation point of unremoved oil film region for the jet leaving a single helicoid (Fig.9 b) at the center of the impinging surface at *Re* = 29800 and 35600. This is attributed to the formation of an intense axial recirculation zone with increased swirling effect even at a higher Reynolds number. For the jet with double helicoids, a stagnation region of unremoved oil film which extends in the *X* plane and two jet impingement sections of oil film removed region are observed (Fig.9 c) and the extent is significant at *Re* = 35600. On the other hand, there appears three impingement sections for triple helicoid insert which extend outward in radial direction away from the stagnation regions and the extent of the impinged area associated is relatively higher on comparison with other types of vanes (Fig. 9 d) which can be substantiated by the Nusselt number distribution presented for triple vanes for Reynolds numbers of 29800 and 35600 (Fig.7d).

At Reynolds numbers of 11200 and 18400 the change in the flow pattern is essentially negligible as the separation distance (*H/D* = 3) increases for single, double and triple vanes fig.10 b, c, d. This is attributed to swirling jet losing its momentum at increased separation distance particularly at lower Reynolds numbers. This fact has also been reported by Yang *et al.* (2010) in their study stating the existence of reverse flow streams for jet at minimum jet exit distances (0.5. and 2.1) and the streams merge to form a single one

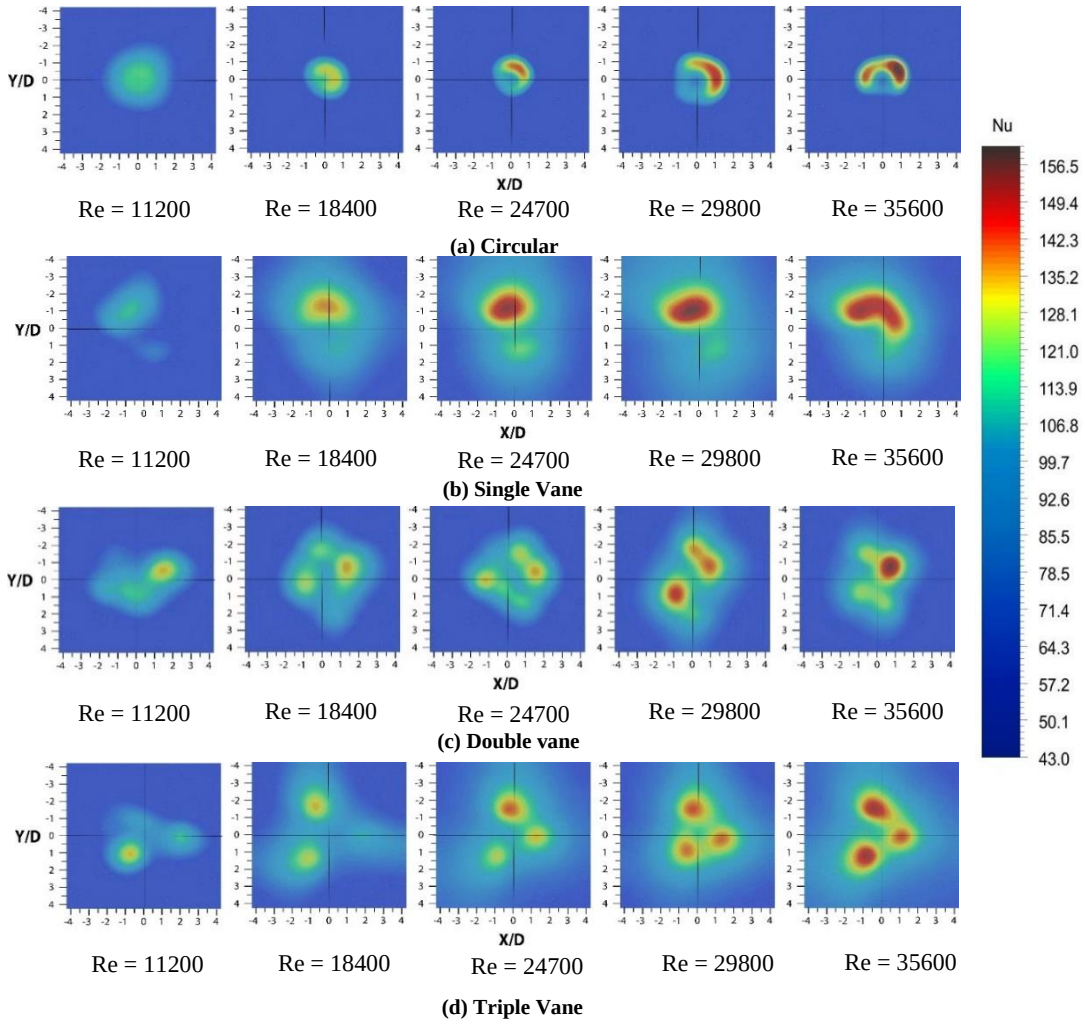

Fig. 7. Nusselt number variation on TLC sheet for circular and swirling jets at *H/D* = 2.

aligning with jet axis with the increase in target surface distance for S = 0.92 at Re = 7000. At Reynolds numbers of 29800 and 35600, the presence of an oil zone at the target surface is particularly noticeable for triple vane (Fig. 10 d) forming an intense axial recirculation zones.

5. NUMERICAL RESULTS

5.1 The axial component of velocity

The axial component of velocity at H/D =1-4 is presented in Fig. 11. In the stagnation area, the swirling jet's axial velocity component is less than zero, increases at $0.57 < r/D < 0.97$ for single vane and $0.63 < r/D < 0.97$ for double and triple vanes (Fig. 11 a) with higher magnitude (u/Uo = 0.78). The stronger axial momentum of the jet with larger swirl at shorter H/D distance is likely the cause of the higher axial velocity. When the H/D distance is increased to 2, the flow is strongly affected by the rotation of the jet, which results in a bigger recirculation region than when the jet exit distance is 1. At jet exit distance of 2 (Fig. 11b) the velocity increase in the impingement zone is less pronounced. This is attributed to the spread of flow stream. For the jet in the stagnation area at jet exit distance of 2 (Fig. 11b), the negative value of velocity component is a little bit higher, and the drop in velocity component is noticeable. The jet leaving the triple vane produces a relatively lower value of negative axial velocity (u/Uo = -0.256) compared with single (u/Uo = -0.127) and double vanes (u/Uo = -0.153) substantiating the existence of a strong recirculation zone in the stagnation region besides increased axial velocity in the impinging area results from the increased kinetic energy the triple vanes, as seen in Fig. 11 b, conveyed to the fluid at jet exit distance of 2. Compared to jet exit distance of 2 (Fig 11 b), the

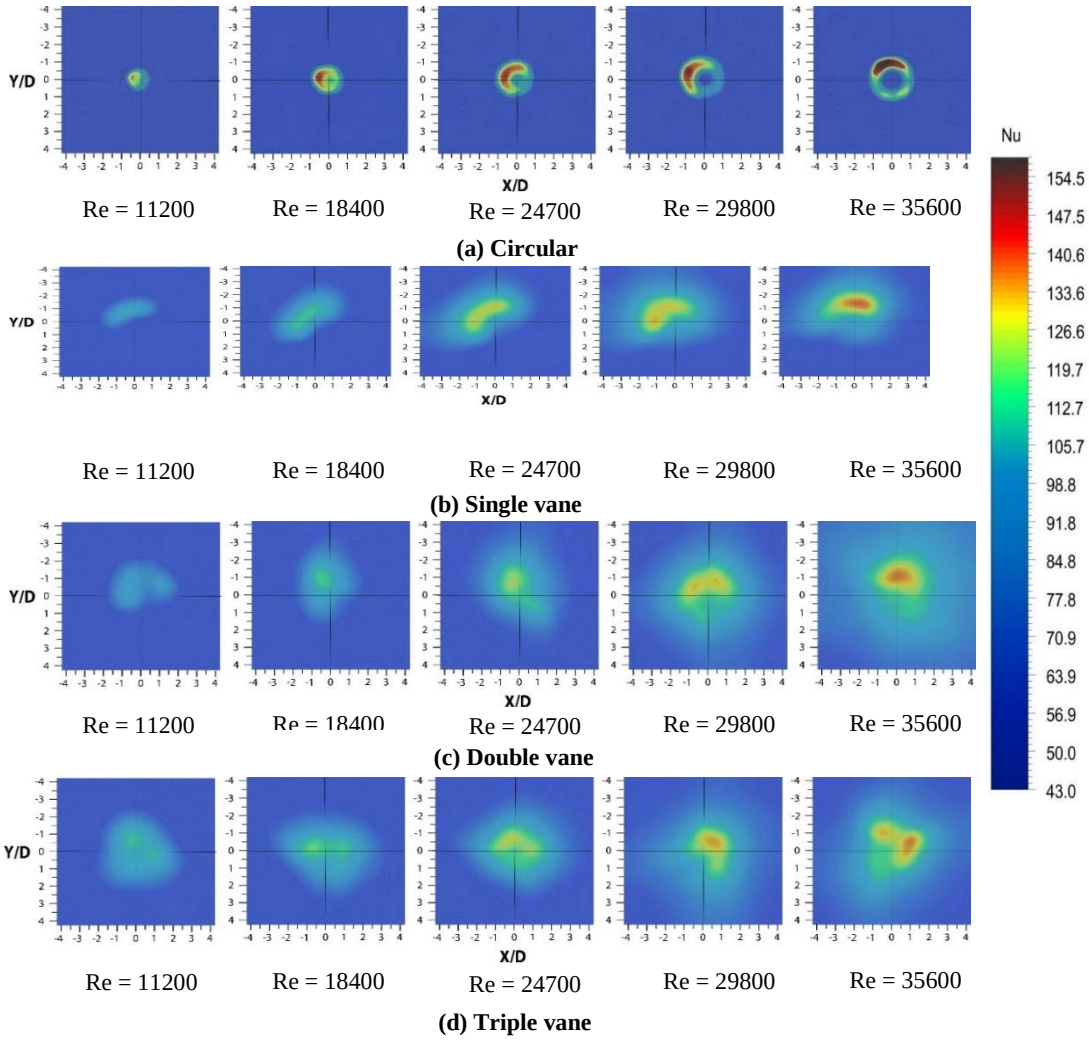

Fig. 8. Nusselt number variation on TLC sheet for circular and swirling jets at *H/D* = 3.

phenomenon of vortex breakup occurs less frequently in the stagnation area for jet exit distance of 3 (Figure 11 c). This results in a smaller magnitude of negative average axial velocity (*u/Uo* = -0.067). Additionally, compared to the region *H/D* = 2, the rise in axial velocity is less pronounced in the range 1.1 < *r/D* < 1.77. This might be because at the increasing target surface distance, the jet loses its initial momentum. The swirling jet leaving the triple vane causes a stronger axial recirculation zone resulting in a relatively lower average negative axial velocity (*u/Uo* = -0.129) in the vicinity of surface compared with single vane (*u/Uo* = -0.079). At *H/D* = 4, the recirculation zone increases radially causing a negative axial component at 0 < *r/D* < 0.97 for single vane and 0 < *r/D* < 1.1 for other vanes besides the peak axial velocity rise being less intense comparing to *H/D* = 3 (*u/Uo* = 0.102) producing lower average axial velocity in the impinging zone (*u/Uo* = 0.083) as shown in Fig.11 d.

The tangential component of velocity at *H/D* =1- 4 is presented in Fig. 11. The velocity component values of the jet (u_t/Uo = 0.454) is larger in at 0 < *r/D* < 0.5. This is due to the larger spreading rate at higher swirl. At *H/D* = 2 (Fig. 12 b), as opposed to jet exit distance of 1, the jet loses its energy, resulting in a sharp drop in velocity (u_t/Uo = 0.381) at *r/D* values between 0 and 1. At jet exit distance of 2, the higher velocity component is modest when considering the single and double vanes and significant for the triple vane (Fig. 12 b). This is because the increased swirl motion of triple vane. The jet of the double vane is characterized by the moderate values of tangential velocity and its intensity is reduced not as rapid as triple vane upon jet spread (Fig. 12 b and c) for *H/D* = 2 and 3 respectively. The velocity peak for the jets leaving double and triple vanes is about 1.3 and 2.1 times lesser than those obtained with *H/D* = 2. This substantiates the reduced tangential momentum at increased separation distances. While the steep increase

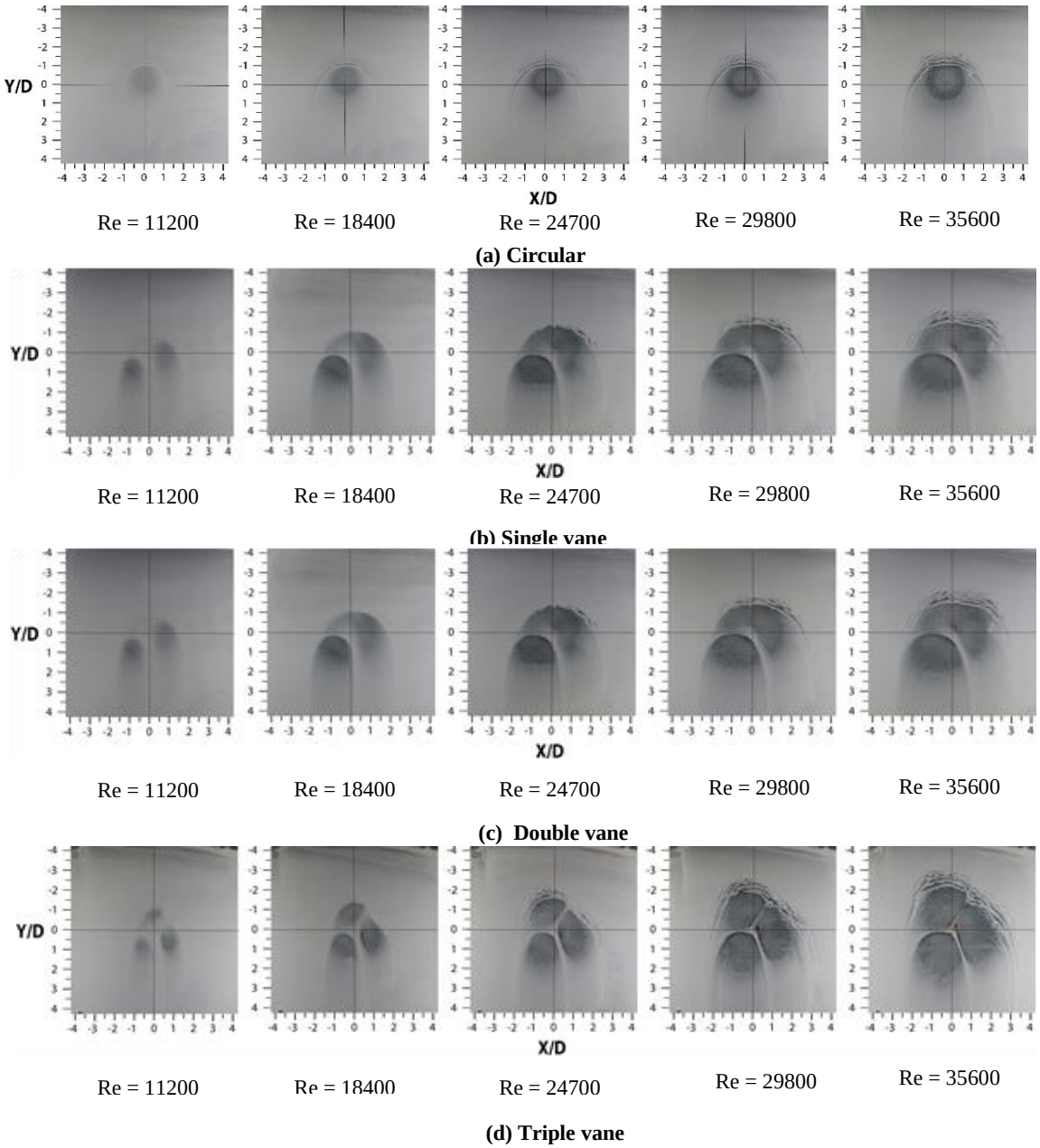

Fig. 9. Flow visualization of round and swirling jets for *H/D* = 2.

in velocity of jet for triple vane is apparent at *r/D* values between 0 and 0.5 at jet exit distance of 2 and 3 (Fig. 12 b and c), the location of maxima (u_t/Uo = 1.358) radially shifts inward towards the jet axis. At jet exit distance of 4, the velocity profiles produced by single and double vanes are nearly flat due to their loss of energy in the impinging and wall jet regions whereas the velocity is marginally higher for triple vanes as shown in Fig.12 d.

5.2 Tangential Velocity Component

5.3 Turbulent kinetic energy variation

The turbulent kinetic energy at *H/D* =1- 4 is presented in Fig. 11. At jet exit distance of 1 for the *r/D* values varying between 0 and 0.7 the jet exhibits an increase in turbulence level (Fig. 13 a) attributed to the higher swirl and no pronounced variation is observed in the distribution of turbulence profile outside at *r/D* > 2,

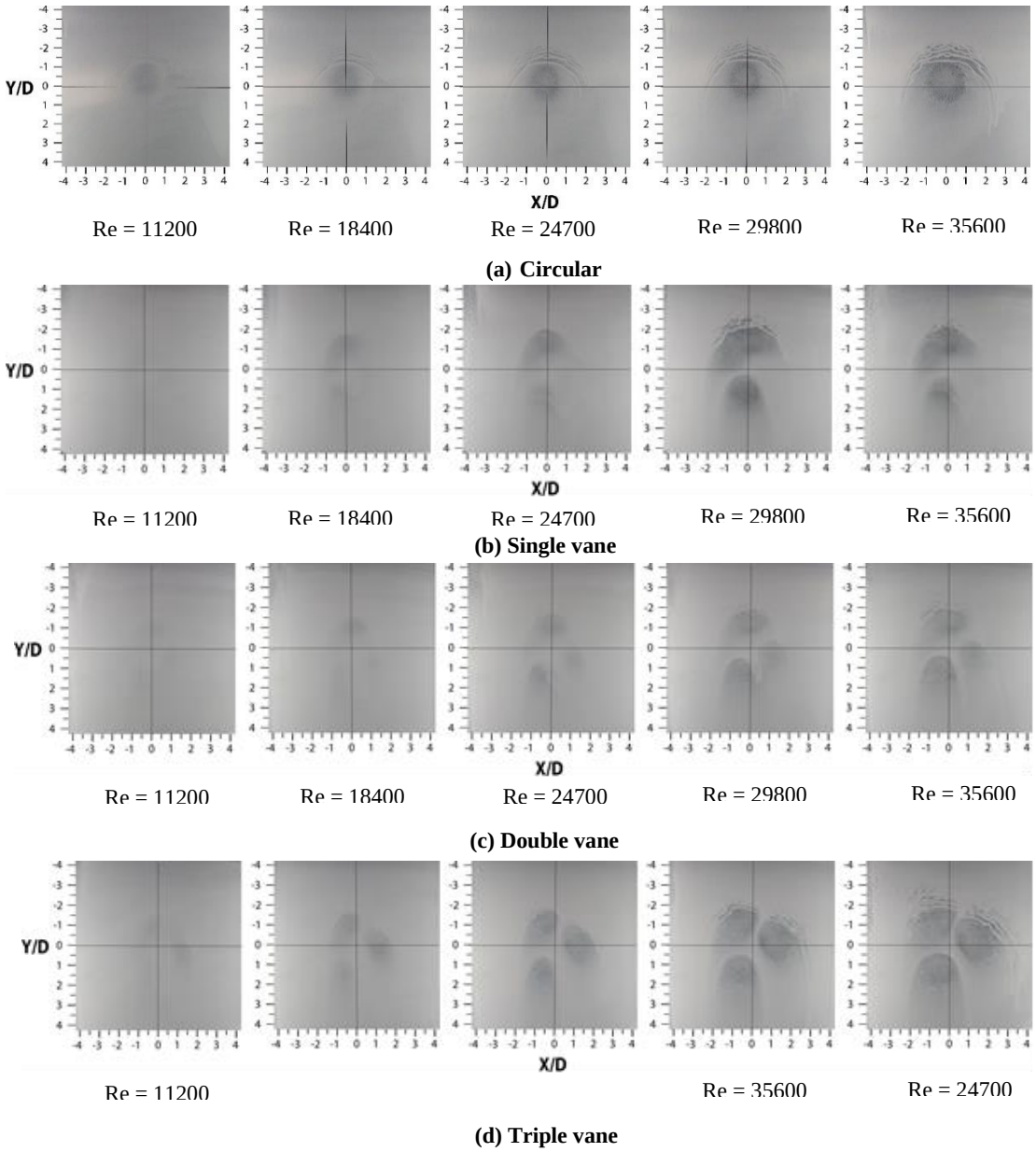

Fig. 10. Flow visualization for circular and swirling jets at *H/D* = 3.

whereas the presence of potential core keeps the turbulence level lower ($u'/U_0^2 = 0.014$) for the circular jet closer to the pipe exit and it increases at *r/D* varying between 1 and 2.4 (Fig. 13 a)

The value of maximum turbulent kinetic energy ($u'/U_0^2 = 0.16$), which describes the swirling jet at *H/D* = 2, is approaching the surface at nearly at *r/D* = 0.9–1.2. Since an increase in turbulence amplitude is more pronounced for the jet leaving triple vane on comparison with other type of vanes, the variation of turbulence better reflects the dependence on the rotating effect. The number of vanes does not noticeably influence the turbulent kinetic energy behavior ($1.5 < r/D < 4$) characterized by wall jet region other than a modest change close to the impinging region for single vane (Fig. 13 b and c) for jet exit distance of 2 and 3. The swirling jet of triple vane significantly influences the intensity of turbulent kinetic energy and the location of its peak (*r/D* = 1.77) in the impinging region (Fig. 13 d) at *H/D* = 4. The peak value of turbulence reaches 1.8 times larger than those obtained with those for single and double vanes respectively. While the increased jet spread for triple vane moves away the peak turbulent intensity to *r/D* = 1.8 for *H/D* = 4 (Fig. 13 d) the jet spread is marginal for

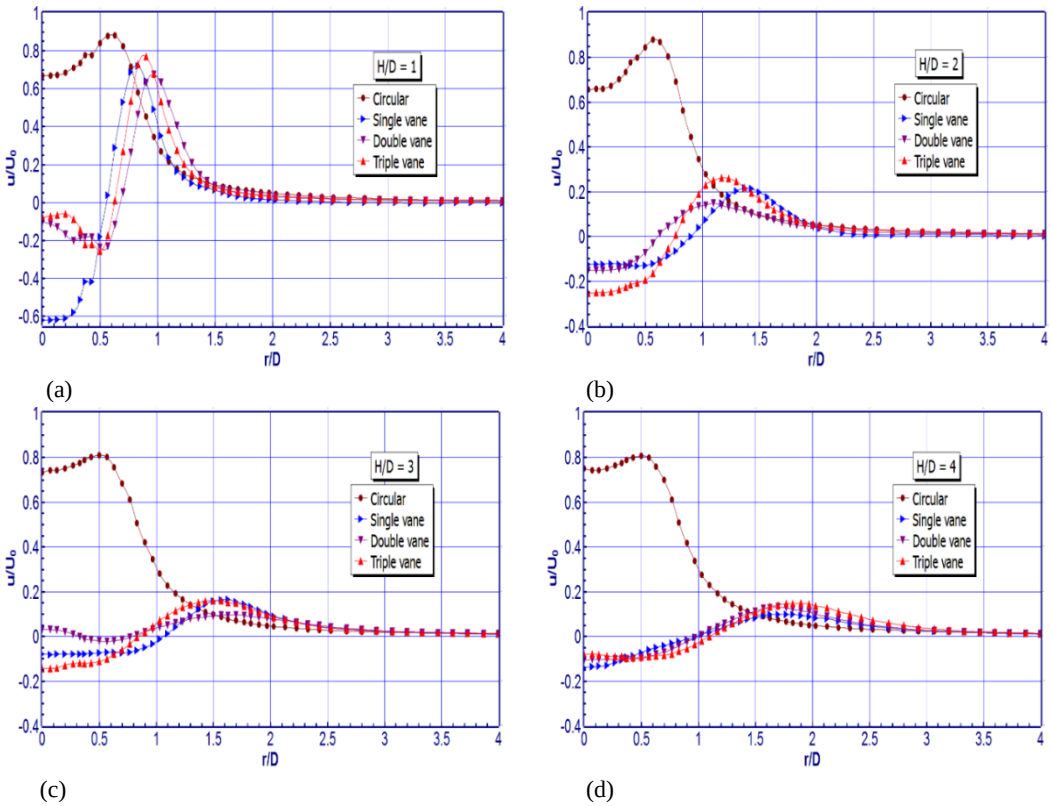

Fig. 11. Axial velocity variation for circular and swirling jets at *Re* = 24700.

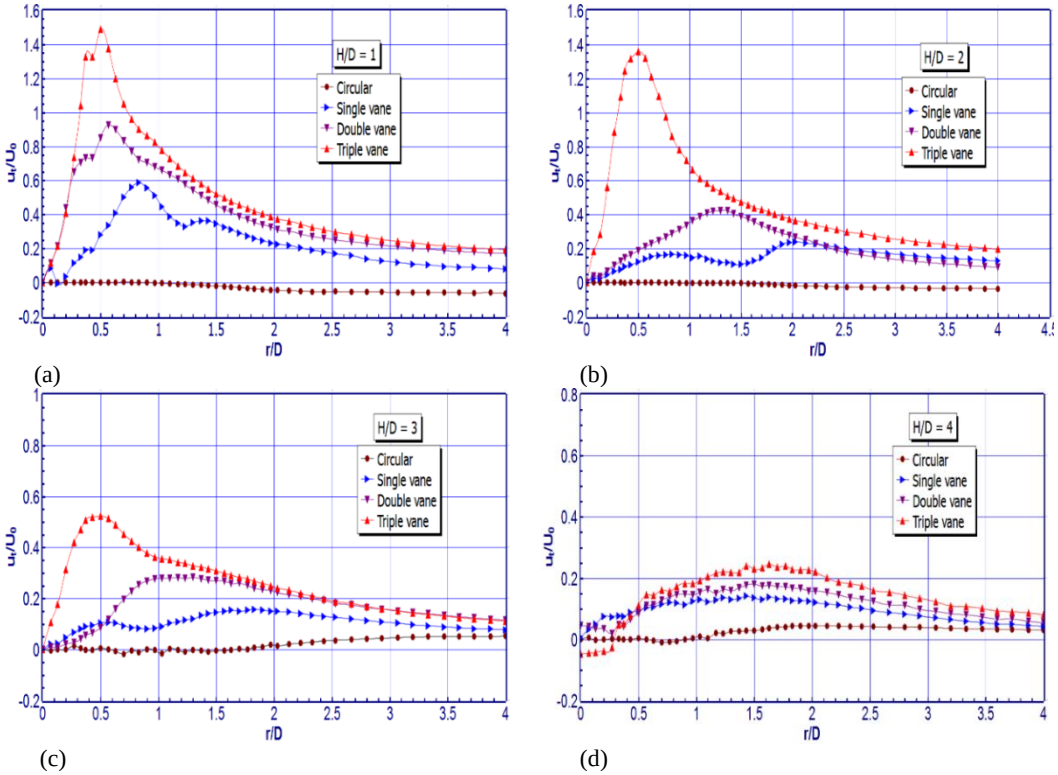

Fig. 12. Tangential velocity variation for circular and swirling jets at *Re* = 24700.

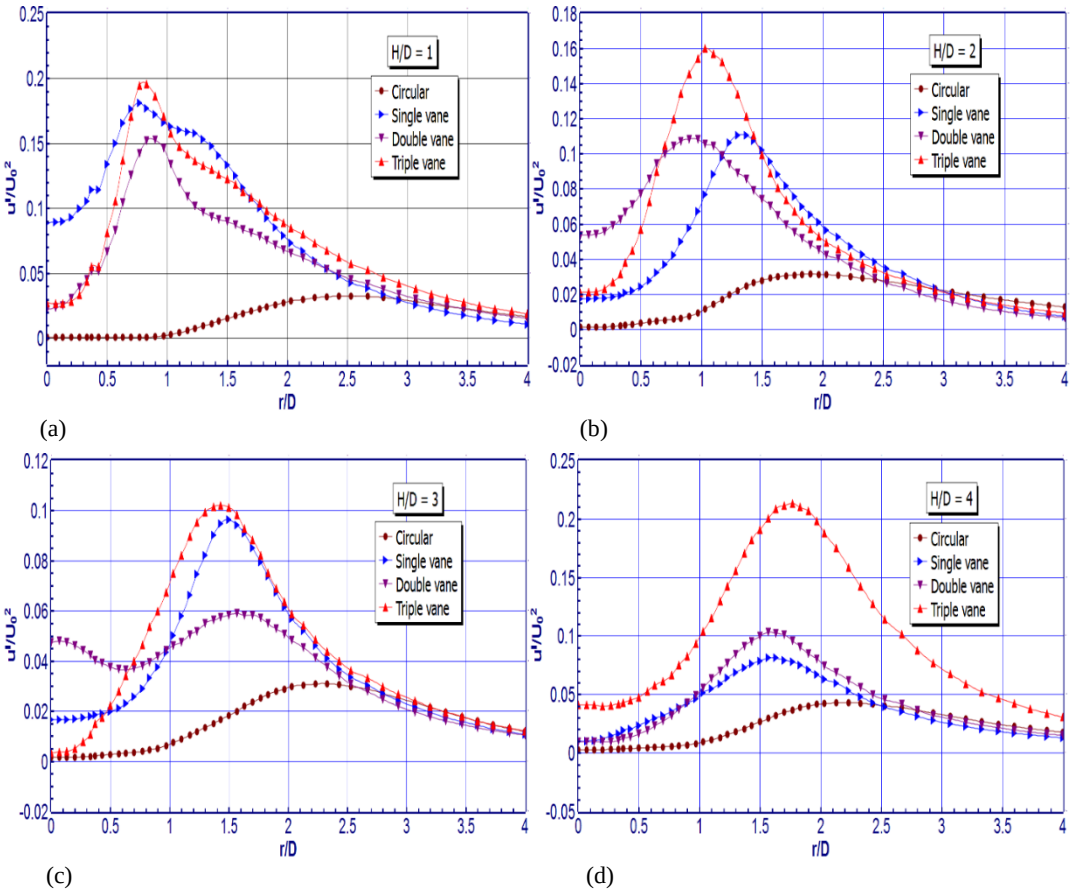

Fig. 13. Turbulent kinetic energy variation for circular and swirling jets at *Re* = 24700.

single and double vanes compared with those obtained for *H/D* = 3.

5.4 Velocity Vector Distribution

The distribution of velocity vector at *H/D* =1- 4 is presented in Fig. 11. The presence of a potential core is visible for circular jet (Fig. 14 a) since the flow is uniform. While the jet flows in downward direction, the fluid near the plate moves radially, and at jet exit distance of 1 where the cross-flow occurs. The influence of cross-flow decreases as the separation distance increases and recirculation zones appear to become larger at jet exit distance of 4. At jet exit distance of 2, the jet shows the existence of two shearing layers as shown in Fig.14 e, m and i. For the swirling jet, which spreads radially in the area at *r/D* value is 1.1 for the vanes, the presence of the outer shear layer is more obvious; yet, aside from the main flow region close to the jet axis, the entire flow structure resembles a circular jet at *H/D* = 1. The flow reversing in the inner shear layer distinguishes the flow pattern of the swirling jet at jet exit distance of 2. The reverse upstream of the vanes is relatively coherent in the inner the flow area, but the many jets of the triple vane type produce more number of recirculation area at *H/D* = 2 (Fig. 14), resulting in an incongruent flow profile in the inner zone and higher turbulence. At *H/D* = 3, the shear layers grow in the region between jet exit and impinging surface and the shear layer influencing over the outer flow is significant as the stronger secondary vortices roll up before the wall jet region and it seems noticeably larger in the case of triple helicoid (fig.14 o). The work by Fenot *et al.* (2015) reporting the emergence of shear layer and root mean square of velocity variations at r/D = 0.7 for *H/D* = 3 at *Re* = 23000 supports this finding. At *H/D* = 4, the shear layer appears similar among the swirling jet and it can be seen that the variation between the flow fields is less visible noticeably on the vicinity of the surface corresponding to $0 < r/D < 2$ as shown in Fig.14 h, l and p). However, the swirling jet's shear layer becomes more evident at *H/D* = 4, supporting its swirl momentum. The reverse flow in the inner shear layer of the swirling jet may reduce the velocity values at downstream of main jet compared with those encountered in the circular jet which is principally due to the tangential velocity component and greater entrainment of ambient air.

6. COMPARISON OF RESULTS

The axial component of velocity variation of the fluid stream (Fig. 15) as determined by the current investigation for *H/D* = 2 is compared with results from

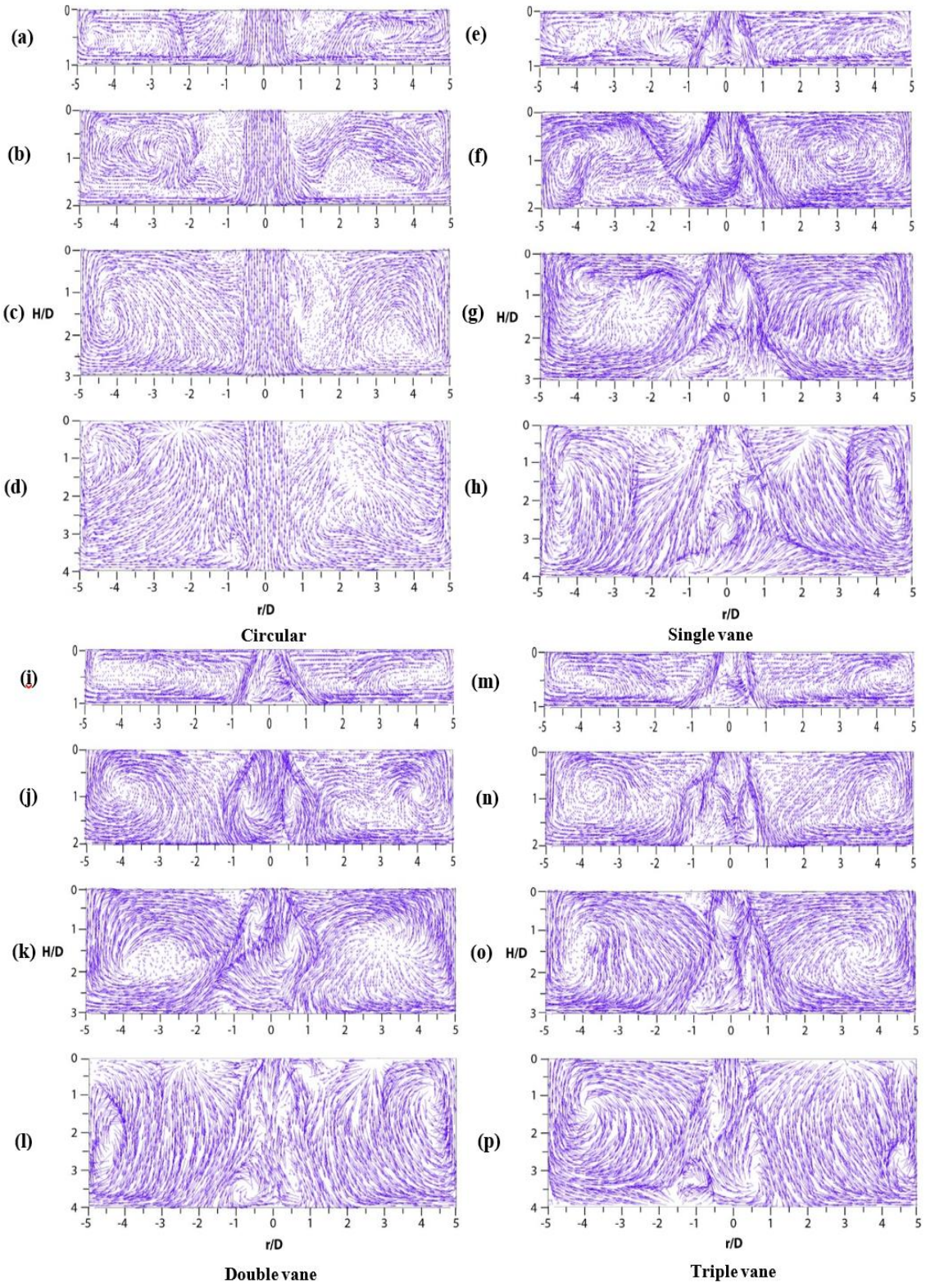

Fig. 14. Velocity vector for circular and swirling jets at *Re* = 24700.

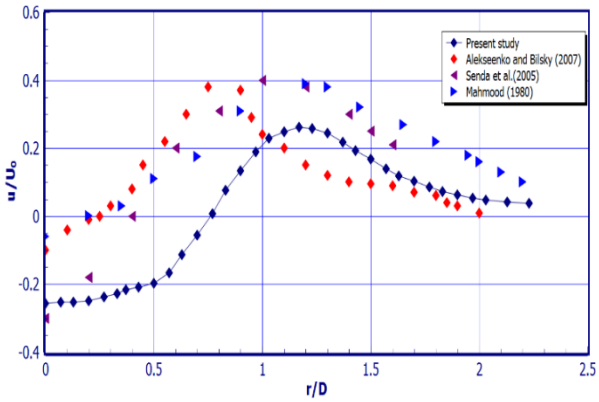

Fig.15. Comparison of axial velocity of swirling jet for *Re* = 24700 at *H/D* = 2 with literature data.

earlier studies. The axial velocity varies between -0.256 and 0.003 at 0 < *r/D* < 2.23. The obtained values fairly agree with the literature in the impinging as well as in the wall jet regions. The axial velocity varies between -0.1 and 0.01 at 0 < *r/D* < 2.23 for Alekseenko and Bilsky (2007). While the variation is between -0.3 and 0.21 in the region 0 < *r/D* < 1.6 for Senda *et al.* (2005). The axial velocity variation is between -0.06 and 0.1 in the region 0 < *r/D* < 2.2 for Mahmood (1980). On comparison with the mean values, the deviation is 23.4% at 0 < *r/D* < 1.1 and it is 12.21% at 1.17 < *r/D* < 2.03.

7. CONCLUSION

The following conclusions are drawn from the experimental and numerical analysis on flow and heat transfer on swirling jet. At the centre of the target surface, the number of vanes significantly influences the formation of axial recirculation zones as it is seen that relatively lower value of Nusselt number for triple helicoids. The jet leaving the triple vane produces a relatively higher value of negative axial velocity (*u/Uo* = -0.207) compared with single (*u/Uo* = -0.147) and double (*u/Uo* = -0.093) vanes substantiating the existence of a strong recirculation zone at 0 < *r/D* < 0.5. When a swirling jet in the stagnation zone, the phenomena of vortex breakup is slightly less for *H/D* = 3 causing a relatively lower magnitude of negative axial velocity (*u/Uo* = -0.067) compared with *H/D* = 2 (*u/Uo* = -0.164). When compared to *H/D* = 2, the velocity peak for the jets of double and triple vanes is 2.1 times smaller than those produced with *H/D* =3. This phenomena supports greater spreading rate at larger jet exit distance.

REFERENCES

Ahlers, G., D. S. Cannell, L. I. Berge and S. Sakurai (1994). Thermal conductivity of the nematic liquid crystal 4-*n*-pentyl-4'-cyanobiphenyl. *Physical review E* 49, 545-553.

Alekseenko, S. V. and A. V. Bilsky (2007). Experimental study of an impinging jet with different swirl rates. *International Journal of Heat and Fluid Flow* 28 (6), 1340-1359.

Bentarzi, F., A. Mataoui and M. Rebay (2019). Effect of Inclination of Twin Jets Impinging a Heated Wall, *Journal of Applied Fluid Mechanics* 12 (2), 403-411.

Cafiero, G., S. Discetti and T. Astarita (2014). Heat transfer enhancement of impinging jets with fractal generated turbulence. *International Journal of Heat and Mass Transfer*, 75: 173-183.

Chandramohan, P., S. N. Murugesan and S. Arivazhagan (2017). Heat Transfer Analysis of Flat Plate Subjected to Multi- Jet Air Impingement using Principal Component Analysis and Computational Technique. *Journal of Applied Fluid Mechanics* 10 (1), 293-306.

Chung, Y. M and K. H. Luo (2002). Unsteady Heat Transfer Analysis of an Impinging Jet. *Journal of Heat Transfer* 124(6), 1039-1048.

Eiamsa-ard S., K. Nanan and K. Wongcharee (2015). Heat transfer visualization of co/counter-dual swirling impinging jets by thermo chromic liquid crystal method. *International Journal of Heat and Mass Transfer* 86, 600- 621.

Fenot, M, E. Dorignac and G. Lalizel (2015). Heat transfer and flow structure of a multichannel impinging jet. *International Journal of Thermal Sciences* 90, 323-338.

Fleischer, A. S., K. Kramer and R. J. Goldstein (2001). Dynamics of the vortex structure of a jet impinging on a convex surface. *Experimental Thermal Fluid Science* 24, 169-175.

Geers, L. F. G., M. J. Tummers, T. J. Bueninck and K. Hanjalic (2008). Heat transfer correlation for hexagonal and in-line arrays of impinging jets. *International Journal of Heat and Mass Transfer* 51(21), 5389-5399.

Gioacchino C., S. Discetti and T. Astarita (2014). Heat transfer enhancement of impinging jets with

fractal-generated turbulence, *International Journal of Heat and Mass Transfer* 75, 173–183.

Goldstein, R. J., and J. F. Timmers (1982). Visualization of heat transfer from arrays of impinging jets. *International Journal of heat and Mass Transfer* 25(12), 1857-1868.

Gupta, A. K., D. G. Lilley and N. Syred (1984). *Swirl Flows*. Abacus Press, Massachusetts, USA.

Holman, J. P. (2002). *Heat Transfer*. Eight SI metric edition, Tata McGraw- Hill, India.

Huang, L. and M. S. El-Genk (1998). Heat transfer and flow visualization experiments of swirling, multi-channel and conventional impinging jets. *International Journal of Heat and Mass Transfer* 41 (3), 583-600.

Huang, Y. and V. Yang (2005). Effect of swirl on combustion dynamics in a lean- premixed swirl-stabilized combustor. *Proceedings of the Combustion Institute* 30, 1775 -1782.

Ianiro, A. and G. Cardone (2012). Heat transfer rate and uniformity in multichannel swirling impinging jets. *Applied Thermal Engineering* 49, 89-98.

Ichimiya, K. and K. Tsukamoto (2010). Heat Transfer characteristics of a swirling laminar impinging jet. *Journal of Heat Transfer* 132 (1), 1-5.

Illyas, S. M., B. R. Ramesh Bapu and V. V Subba Rao (2019). Experimental Analysis of Heat Transfer and Multi Objective Optimization of Swirling Jet Impingement on a Flat Surface. *Journal of Applied Fluid Mechanics* 12 (3), 803-817.

Kinsella, C., B. Donnelly, T. S. O'Donovan and D. B. Murray (2008). Heat transfer enhancement from a horizontal surface by impinging swirl jets. *Fifth European Thermal Sciences Conference*. Netherland, UK.

Liu, Z., J. Li and Z. Feng (2015). Numerical study of swirl cooling in a turbine blade leading edge model. *Journal of Thermo Physics and Heat Transfer* 29 (1), 66-178.

Lytle, D. and B. W. Webb (1994). Air jet impingement heat transfer at low nozzle-plate spacing. *International Journal of Heat and Mass Transfer* 37 (12), 1687-1697.

Mahmood, M. (1980). Heat transfer from swirling impinging jets. Ph.D thesis, *Cranfield Institute of Technology*, Cranfield, UK.

Park, S. H. and H. D. Shin (1993). Measurements of entrainment characteristics of swirling jets. *International Journal of Heat and Mass Transfer* 36 (16), 4009 - 4018.

Qiu, D., L. Luo, S. Wang, B. Sunden and X. Zhang (2019). Analysis of heat transfer and fluid flow of a slot jet impinging on a confined concave surface with various curvature and small jet to target spacing. *Heat Transfer and Fluid Flow* 29, 2885-2910

Senda, M., K. Inaoka, D. Toyoda and S. Sato (2005). Heat Transfer and Fluid Flow Characteristics in a Swirling Impinging Jet. *Heat Transfer Asian Research* 34 (5), 324 - 335.

Sheen, H. J., W. J. Chen, S. Y. Jeng and T. L. Huang (1996). Correlation of Swirl Number for a Radial-Type Swirl Generator. *Experimental Thermal and Fluid Science* 12, 444 - 451.

Shukla, A. K. and A. Dewan (2017). Convective heat transfer enhancement using slot jet impingement on a detached rib surface *Journal of Applied Fluid Mechanics*, 10 (6), 1615-1627

Tang, Z. G., F. Deng, S. C. Wang and J. P. Cheng (2021). Numerical simulation of flow and heat transfer characteristics of a liquid jet impinging on a cylindrical cavity heat sink. *Journal of Applied Fluid Mechanics* 14, 723 – 732.

Tangirala, V., R. H. Chen and J. F. Driscoll (1987). Effect of Heat Release and Swirl on the Recirculation within Swirl- Stabilized Flames. *Combustion Science and Technology* 51, 75 - 95.

Tannehill, J. C., D. Anderson and R. H. Pletcher (1997). *Computational Fluid Mechanics and Heat Transfer*. Second Edition, Taylor and Francis.

Versteeg, H. K. and W Malalasekara (1995). An Introduction to Computational Fluid Dynamics: *The Finite Volume Method*, Longman Scientific and Technical Publishers, England

Wannassi, M. and F. Monnoyer (2015). Fluid flow and convective heat transfer of combined swirling and straight impinging jet arrays, *Applied Thermal Engineering* 78, 62 -73

Yang, H. Q., T. Kim, T. J. Lu and K. Ichimiya (2010). Flow structure, wall pressure and heat transfer characteristics of impinging annular jet with/without steady swirling. *International Journal of Heat and Mass Transfer* 53(19), 4092-4100.

Yazdabadi, P. A., A. J. Griffiths and N. Syred (1994). Characterization of the PVC phenomena in the exhaust of a cyclone dust separator. *Experiments in Fluids* 17, 84 - 95.

Zuckerman, N. and N. Lior (2006) Jet impingement heat transfer: physics, correlations, and numerical modeling. *Advances in Heat Transfer* 39, 565-631